Research Article

Graphene Oxide Nanoadsorbent for the Removal of Fluoride Ion from Groundwater: Adsorbent Performance and Adsorption Mechanism

Bayisa Meka Chufa [iD],[1] Bedasa Abdisa Gonfa [iD],[1] and Teketel Yohannes Anshebo [iD][2]

[1]*Department of Applied Chemistry, School of Applied Natural Science, Adama Science and Technology University, P.O. Box 1888, Adama, Ethiopia*
[2]*Department of Chemistry, School of Natural Science, Addis Ababa University, P.O. Box 1176, Addis Ababa, Ethiopia*

Correspondence should be addressed to Bayisa Meka Chufa; nathan.meka@astu.edu.et

The deterioration of the quality of groundwater by fluoride is the cause of shortage of drinking water supply in the rift valley region. Most people living in the rural areas are using groundwater as the source of their potable water; however, it is contaminated with high concentrations of fluoride ion above the permissible level. Hence, this study was designed to investigate the adsorption of fluoride from groundwater by graphene oxide (GO) under specific conditions, such as: agitation rate of 120 rpm, contact time of 90 minutes, adsorbent dosage of 0.42 mg/L, initial fluoride concentration of 10 mg/L, and pH of 6.8. The result obtained showed 99.3% fluoride removal from the NaF prepared solution and 91.6% fluoride removal from the real sample. The retained properties of GO after adsorption observed on UV–Vis analysis confirmed that the adsorbent can be recyclable. The result obtained also showed that the adsorption kinetics with the coefficient of determination (R^2) for pseudo-second order (SSO) and pseudo-first order (SFO) were 0.99 and 0.96, respectively. Based on these results, the adsorption of fluoride onto GO is a pseudo-second-order kinetics type. According to the result, the Freundlich isotherm model showed a good fit to the experiment with R^2 (0.99). The adsorption capacity of the adsorbent was found to be 301.43 mg/g. Hence, this study showed that GO is the preferred adsorbent for the removal of fluoride from groundwater.

1. Introduction

The demand for pure drinking water supply is growing rapidly as a result of continuous increase of the world population [1]. Most people living in the rural areas are using groundwater as the main source for drinking. Usually, groundwater has high concentrations of fluoride due to the dissolution of some mineral ores [2–4]. Although groundwater possesses good microbiological and biological properties, it is contaminated with some toxic chemicals, which may pose serious health effects to living organisms [5]. Besides its advantages at its permissible concentration, fluoride causes significant health problems [6]. The World Health Organization (WHO) set the recommended upper limit of fluoride ion concentration to be consumed in food to

not be more than 1.5 mg/L [7]. However, fluoride ion concentrations in some African rift valleys' groundwater were recorded to be greater than this limit by far. Most of the east African regions that extend from the Jordan valley down through Sudan, Ethiopia, Kenya, Uganda, and Tanzania were reported to have maximum fluoride ion concentration [8–10].

Reports showed that the Ethiopian rift valley groundwater contains fluoride concentration much higher than the allowed level [11, 12]. The concentration of fluoride ion for Ethiopian rift valley lakes, such as Lake Shala and Lake Abijata, was recorded to be 264 mg/L and 202.4 mg/L, respectively [11]. The increase in the concentration of fluoride ion in groundwater along the course of the river flow is due to the existence of acidic rocks lengthways across and recent

volcanic hot eruptions [13–15]. The landforms of the Ethiopian rift valley exist in a variety of terrain that is significantly important to the enrichment of fluoride in groundwater [16]. If present beyond the permissible values, fluoride causes significant health disorders. According to some research findings, the ingestion of food/water with fluoride concentration 1.5–3 mg/L causes dental fluorosis, 3.5–9 mg/L causes skeletal fluorosis, and longtime ingestion of fluoride with concentrations greater than 10 mg/L causes an irreversible damage to the bones called bone immobility or crippling fluorosis [17–19].

Although defluoridation of water is difficult and expensive, a number of methods have been applied [20]. The most common defluoridation techniques reported were ion-exchange, precipitation, nanofiltration, electrochemical methods, reverse osmosis, and adsorption [21, 22]. Among these, adsorption is a quite effective and efficient method because of the ease of operations, less time and space consumption, ease of material availability, ecofriendly, and cost effectiveness [23–25]. The groundwater sources serving as drinking water supply for a community living in "Dugda-Bora district of Oromia regional state, Ethiopia" contain high concentrations of fluoride, which caused tremendous health effects and even death [26, 27]. The above-mentioned defluoridation techniques were applied [28, 29], but the problem was not yet resolved.

Activated carbon has been used as adsorbent due to its excellent adsorption capacity for a wide range of contaminants; however, its application is restricted recently due to the high production cost and difficulties in recyclability [30, 31]. Carbon nanotubes (CNTs) and graphene-based materials (GBMs) have been developed as an alternative to conventional adsorbents [32]. Researchers used CNTs to build new adsorbents because of their high surface area, non-corrosive nature, presence of oxygen-containing functional groups, tunable surface chemistry, and scalable production [33]. However, graphene-based nanomaterials were found to be more advantageous than CNTs in adsorption activities due to: (1) The availability of two basal planes of single-layered graphene materials for pollutant adsorption, unlike the inner walls of CNTs that are not accessible by the adsorbates. (2) The ease of manufacturing graphene-based materials by simple chemical exfoliation of graphite without using complex apparatus or metallic catalysts; the produced graphene-based material is free of catalyst residues such that no further purification steps are needed [34]. (3) The as-prepared GO possesses a large number of oxygen-containing functional groups that are likely responsible for the adsorption of ionic pollutants, and no additional acid treatments are needed to impart a hydrophilic character and reactivity unlike CNTs.

In this work, we explored the application of graphene-based nanomaterial as an adsorbent for the removal of fluoride ions from aqueous solutions. Besides, we described the key adsorption mechanisms performed by GO. A novel experimental method of studying the mechanisms by which the adsorbent was continuously adsorbing the adsorbate without saturating the active site was also described. Based on recent discoveries that the graphene oxide surface can be modulated by molecules assembled on its surface and pH optimization, we have studied fluoride adsorption using GO by optimizing pH.

2. Materials and Methods

2.1. Batch Adsorption Study. All the chemicals and reagents used throughout this study were of analytical grade. 5 borosilicate glasses of 150 mL containing 50 mL of known concentration of fluoride solution (10 mg/L) at different pH, contact time, and adsorbent dosage were prepared at room temperature. The filtrate was collected by filtering the solution using Whatman filter paper and was stored for the residual fluoride analysis using photometer measurement. The adsorbent was washed repeatedly using doubly distilled water and was used to check its recyclability and reusability. The stock solution of fluoride was obtained by dissolving 2.21 g of NaF salt in 1 L of distilled water. 0.1 N of NaOH and H_2SO_4 were used to adjust the pH of the sample. The fluoride concentration was measured by (HACH photometer instrument, Model Number DR6000; USA). The equilibration for the adsorption experiment was maintained by continuous shaking of the mixtures using a rotary shaker. The percentage adsorption (A), percentage degradation (Φ), and adsorption capacity at equilibrium $q_{e\exp}$ (mg/g) were calculated as:

$$A = \frac{C_0 - C_t}{C_0} * 100,$$

$$\phi = \frac{C_0 - C_t}{C_0} * 100, \tag{1}$$

$$q_{e\exp} = \frac{(C_0 - C_t)V}{W},$$

where C_0 and C_t are the F^- concentration before and after adsorption, V (L) is the volume of the F^- solution taken, and W (g) is the weight of the adsorbent used.

2.2. Synthesis of Graphene Oxide (GO). In our preceding work, we reported the novel and simplest synthesis method of GO by mixing a mixture of sulfuric/phosphoric acids in a 9 : 1 ratio and graphite/$KMnO_4$ in a 6 : 1 ratio. In the course of the synthesis, different colors which confirmed the formation of GO were observed [35]. Graphene-based nanomaterials synthesized this way and characterized using different instruments were used in the present work for the removal of fluoride ions from aqueous solutions.

2.3. Theoretical Models

2.3.1. Study of Adsorption Kinetics. The following equations were used to study the fluoride adsorption kinetics and rate-controlling steps. Pseudo-first-order (SFO), pseudo-second-order (SSO), and diffusion model equations were denoted by (2), (3), (12), and (13), respectively.

$$\log(q_e - q_t) = \log q_e {}^{-\left(k_f t/2.303\right)}, \qquad (2)$$

$$\frac{t}{q_t} = \frac{1}{q_e^2 k_s} + \frac{t}{q_e}, \qquad (3)$$

where k_f–SFO rate constant (g/mg, min), k_s–SSO rate constant (g/mg, min)

The precision of the adsorption kinetics model fitting was checked by standard deviation (SD), coefficient of determination (R^2), and nonlinear chi-square (χ^2), equation.

$$\chi^2 = \sum \frac{\left(q_{e\exp} - q_{ecal}\right)^2}{q_{e\,cal}^2}. \qquad (4)$$

2.3.2. Adsorption Isotherm. In this work, four adsorption isotherm models (Langmuir, Freundlich, Tempkin, and Dubinin–Radushkevich, D–R) were used to analyze the equilibrium relationship between the adsorbent and the adsorbate. The following equations (5), (7)–(9) describe the Langmuir, Freundlich, Temkin, and Dubinin–Radushkevich, D–R isotherm models, respectively.

$$q_e = \frac{C_e * K_L * q_m}{1 + K_L * C_e}. \qquad (5)$$

The Langmuir constant shows the free energy (ΔG) for the process of adsorption which can be obtained from:

$$\Delta G = -RT \ln K_L. \qquad (6)$$

The Langmuir equilibrium parameter R_L is described as: $R_L = 1/1 + (1 + K_L C_0)$, C_0 is the initial adsorbate concentration. If $R_L > 1$, it is an unfavorable process; if $R_L < 1$, the process is favorable, and if $R_L = 0$, the adsorption process is irreversible.

$$q_e = K_{F*} C_e^{1/n_F}, \qquad (7)$$

where q_e is the amount of fluoride adsorbed per unit mass of the adsorbent (mg/g), C_e is the equilibrium concentration (mg/L), q_m is the maximum adsorption capacity of the adsorbent(mg/g), and K_L & K_F are the Langmuir and Freundlich adsorption rate constants (L/mg) and (mg/g (L/mg)$^{1/nF}$), respectively. $1/n$ is the adsorption intensity.

The Temkin model, which takes into account the interactions of the adjacent adsorbate ions and assumes the heat of adsorption decreases linearly with increasing covered surface, is expressed as:

$$q_e = \frac{RT}{b} \ln k_T + \frac{RT}{b} \ln C_e, \qquad (8)$$

where b is heat of sorption (in Joules per mole) and K_T is the Tempkin equilibrium constant (in litter per milligram); R is the universal gas constant and T is the absolute temperature.

The other isotherm model that relates the adsorption characteristics with the available porosity and applied only to porous materials is the D–R model. This model is usually applied to solutions containing intermediate to high concentrations and is expressed as:

$$\ln q_e = \ln q_s - K_{DR} \varepsilon^2, \qquad (9)$$

where q_s is the theoretical adsorption saturation capacity (in milligram per Gram), K_{DR} is the D–R isotherm constant (in mole^2 per joule^2), and the term ε is obtained from the expression:

$$\varepsilon = RT \ln\left[1 + \frac{1}{C_e}\right]. \qquad (10)$$

The mean free energy (E) for adsorption can be calculated as:

$$E = \frac{1}{\sqrt{2K_{DR}}}. \qquad (11)$$

2.3.3. Diffusion Studies. The adsorption mechanisms were thoroughly explained using models–an intraparticle diffusion model, which employs the Weber Morris plot, i.e., q_t versus t shown in equation (12), and a particle diffusion model based on the Chanda plot, i.e., $\ln(1 - C_t/C_e)$ versus t as shown in equation (13).

$$qt = k_{id} t^{0.5} + C_i, \qquad (12)$$

where k_{id} (mgg^{-1}min$^{0.5}$) is the rate constant of stage i and C_i is the thickness of the boundary layer; it is constant.

$$\ln\left(1 - \frac{C_t}{C_e}\right) = -k_p t, \qquad (13)$$

where k_p (mgg^{-1}min^{-1}) is the rate constant.

These two models are used to evaluate if the retention process is controlled by an intraparticle diffusion model or a particle diffusion model.

3. Results and Discussion

3.1. Physicochemical Properties of the Sample. The physicochemical properties of the Dugda-Bora groundwater with maximum fluoride content were analyzed and the results were presented in Table 1.

3.2. Synthesis of GO Nanoadsorbent. Immediately as the acid mixture was poured into a beaker containing a mixture of graphite and potassium permanganate, a deep green thick solution was formed which depicted the production of dimanganese heptoxide (Mn_2O_7) accompanied with the rise in temperature from room to 50°C [35, 36]. The increase in the temperature of the solution recorded was the indicator of exothermic redox reactions. While continuous stirring and heating of the mixture, the formation of a thick slurry solution was observed, which was later changed into a brown solution with prolonged reactions and this was the confirmation of the formation of GO as it was also reported previously [35–37].

TABLE 1: The physicochemical properties of the Dugda-Bora groundwater with maximum fluoride content.

Parameters	Values
pH	8.5
Conductivity (μs/cm)	3000
Total Hardness (mg/L)	108
F^-(mg/L)	37
SO_4^- (mg/L)	7
Cl^- (mg/L)	4
PO_4^- (mg/L)	0.6
NO_3^- (mg/L)	14.7
HCO_3^- (mg/L)	371

3.3. Characterization of GO Nanoadsorbent

3.3.1. UV–Vis Absorption Analysis. The analysis result of GO using UV–Vis spectroscopy was shown in Figure 1. The UV–Vis spectra of GO depicted an absorption peak at 230 followed by a shoulder at 300 nm. As it can be seen from the spectra of UV–Vis in Figure 1, no signal is observed in the region between 400 and 800 nm. This result shows good responses of GO nanostructure in both ultraviolet and visible regions, which implies the potential of the synthesized material for the application of light-based activities. The maximum absorbance is formed at 230 nm and this is attributed to π–$\pi*$ transitions of the -C=C- bonds in the aromatic rings. The shoulder found at around 300 nm is associated to the edge carbonyl group (C=O) of the rings as was presented in our previous work [35]. Hence, the UV–Vis spectra of GO suggests the presence of a more ordered structure which is due to the retention of carbon rings in the basal planes.

3.3.2. X-Ray Diffraction (XRD). The average crystalline structural properties of GO were determined using XRD techniques. A sharp diffraction peak for GO was observed at $2\theta = 10°$ as shown in Figure 2 and the corresponding layer-to-layer distance (d-spacing) was determined to be 0.87 nm, which is similar to literature value [35, 36]. The XRD patterns showed a larger d-spacing for GO (0.87 nm) than graphite (0.34 nm) [35] and this is attributed to the insertion of a large number of oxygen-containing functional group between the precursor graphite layer from the oxidizer $KMnO_4$ during the oxidation process. Another peak was observed at around $2\theta = 43°$ in this pattern, which is possibly due to the slipping out of the alignment of the layer of GO in the basal plane. Hence, this result confirms the successful synthesis of GO nanostructure.

3.3.3. Fourier-Transform Infrared Spectroscopy (FT-IR). The functional groups and the structure of GO were determined from its FT-IR spectral analysis as shown in Figure 3. The absorption peak recorded was associated with their corresponding functional groups in the basal plane and the edge of the mother GO structure. The broad band observed at 3400 cm^{-1}was for hydroxide groups, the bands at 2850 and 2920 cm^{-1} were for the C–H symmetric and asymmetric stretching frequencies, respectively, the band at
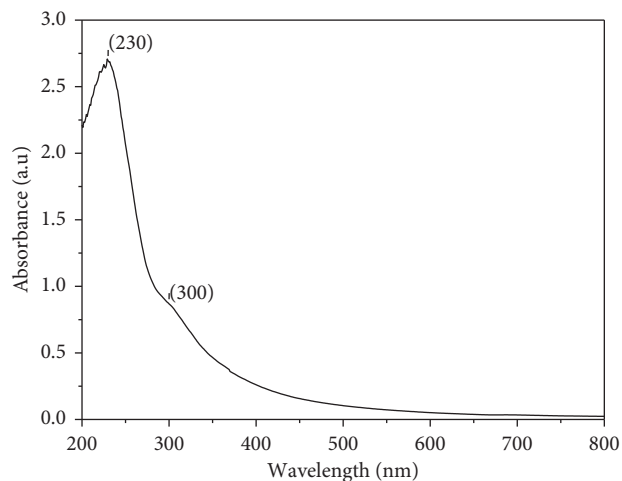

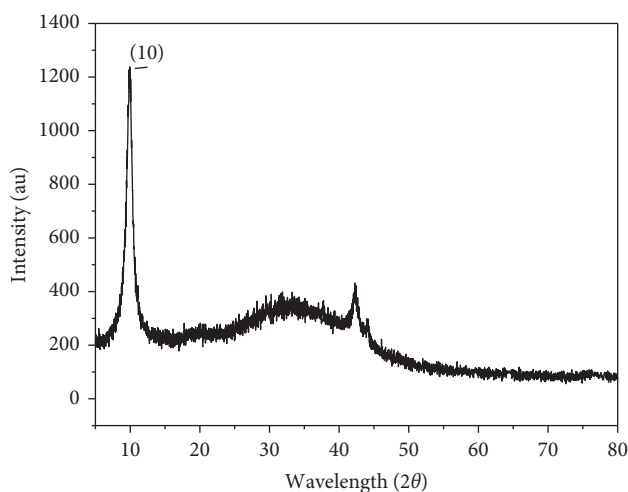FIGURE 1: UV–Vis spectra record of GO.

FIGURE 2: X-ray diffraction patterns of GO.

1735 cm^{-1} was for the C=O carboxyl group, the band at 1623 cm^{-1} was for the C=C of aromatic rings, the band at 1378 cm^{-1} was for the stretching of the C – OH of the carboxylic acids, the band at 1226 cm^{-1}corresponds to the epoxide (C–O) functional groups, and the one at 1051 cm^{-1} was for alkoxy C–OH. Therefore, the presence of these oxygen-containing functional groups in the structure of GO confirmed the successful oxidation of the precursor graphite to produce graphene oxide, whereas the sharp absorption band observed at 1623 cm^{-1} depicted the retaining of C=C in the aromatic ring in GO.

3.3.4. Scanning Electron Microscopy (SEM). The SEM images recorded under different magnifications of the same sample of GO synthesized by slight modifications to the improved method are shown in Figures 4(a)–4(d)). It is evident from these micrographs that GO showed more wrinkles and folds at its edges and agglomerates with two-dimensional sheets like structure shown in Figures 4(b) and 4(c). The GO morphologies given in Figure 4 showed visible
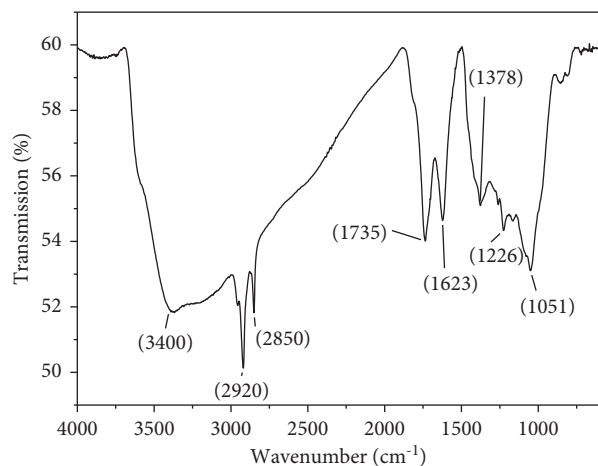
Figure 3: FT-IR spectra of Graphene oxide (GO).

layer arrangements because of the layer expansion due to the insertion of oxygen-containing functional groups, which was also reported in the literature [35, 38]. The multiple lamellar layer structures and independent individual sheets of GO were also observed in the micrographs as shown in Figure 4(d). The thickness of GO observed at the edge is due to the combination of the oxygen-containing functional groups concentrated at the edge than at the middle.

3.3.5. High-Resolution Transmission Electron Microscopy (HR-TEM).
HR-TEM images presented in Figures 5(a)–5(d) support the claims described in SEM, UV–Vis, and XRD that GO synthesized this way has more regular structures. This procedure produces large flakes of GO that are few layers thick indicated by the transparent layers shown in Figures 5(c)–5(d). The sharp diffraction pattern shown in Figure 5(a) depicted the highest crystallinity which implied a more regular carbon framework in the ring structure of GO. The slightly wrinkled morphologies of GO were recorded here as observed in Figure 5(b). Single and double lamellar structure GO sheets were observed in the HR-TEM images, where the size of the lamellar structure was determined to be around $4 \mu m$.

As shown n Table 2, the EDAX analysis confirms that GO contains a major percentage of carbon and oxygen and small amounts of sulfur and chloride, which possibly originated from H_2SO_4 and HCl used during the synthesis, respectively.

3.4. Adsorption Studies

3.4.1. Effect of pH.
The adsorption of anionic pollutants on GO is affected by pH, with the adsorption capacity increasing at lower pH [39]. The behaviour of GO in aqueous solutions is governed by its point of zero charge (pH_{pzc}). When the solution pH is greater than pH_{pzc}, then the GO surface is negatively charged because of the deprotonation of the carboxyl and hydroxyl groups. On the other hand, when the solution pH is less than pH_{pzc}, the GO surface becomes positively charged [23]. Hence, this larger pH_{pzc} value than

the media solution pH is the condition under which we performed our investigations.

The adsorption of fluoride onto GO was determined by varying the pH values from 3 to 11. The hydrogen ion concentration plays a significant role in determining the fluoride ion adsorption capacity of graphene-based nanomaterials. OH^- is the anion competing for the adsorption of F^- because of their similar lattice size and charge. The pH_{pzc} of the adsorbent and the pH of the stock solution were determined prior to carrying out the adsorption activity to be 4.5 and 8.5, respectively. The pH of the mixture solution became around 6.8. Hence, this is a favorable pH value where GO is ready to adsorb the negatively charged anions.

When $pH_{pzc} > pH$, the surface of GO is positively charged and ready to attract negatively charged particles. At this pH, the epoxides across the basal plane and carbonyl, carboxyl at the edge of GO are highly protonated and the total surface of the adsorbent is positively charged. Hence, this is the convenient condition for the fluoride ion to be adsorbed on the GO surface.

The reusability and recyclability of the adsorbent were tested by desorbing the fluoride from the surfaces through acidification of the solution. The optimum pH at which GO adsorbs fluoride ions was obtained to be 6.8. At this pH, 99.3% of fluoride ions obtained from the NaF complex solution and 91.6% of fluoride in the real sample were adsorbed by GO, which is similar to previous reports [21, 22, 26]. The experiment has been performed at the adsorbent dosage of 0.42 mg, fluoride ion concentration of 10 mg/L, agitation speed of 120 rpm, agitation time of 90 minutes, and different pH values 3, 5, 7, 9, and 11 as shown in Figures 6 and 7.

The UV–Vis records of the mixture were taken at different pH values and the result showed that the UV–Vis absorption peak of a complex solution of fluoride ion formed at λ_{max} around 522 was completely removed after adsorption. The result also showed that the behaviour of GO on the absorption spectrum of the UV–VIS record with the λ_{max} value 226 was retained unchanged after the adsorption process as shown in Figure 8.

This depicted the adsorption process is physisorption, and hence the possibility of reusing the adsorbent is high. However, the intensity of the absorption peak of the adsorbent after the adsorption is not consistent. As shown in Figure 8, the intensity of the UV–Vis absorbance spectrum for the solution with pH 9 is maximum, but the adsorption capacity of the adsorbent at this pH is 78%. The exchange capacity of GO for fluoride decreased rapidly for solutions with pH greater than 7 as shown in Figures 6 and 7. The adsorption rates were also found to decrease (as shown by the sharp decrease of the graph) with increasing solution pH beyond 7.

3.4.2. Effects of Contact Time.
By adding the known amount of adsorbent dosage 0.42 mg to each of 50 mL fluoride solution in measuring flasks containing 10 mg/L of initial fluoride concentration, agitated by a digital shaker at 120 rpm, and pH of 6.8 with varying contact time 50, 70, 90,
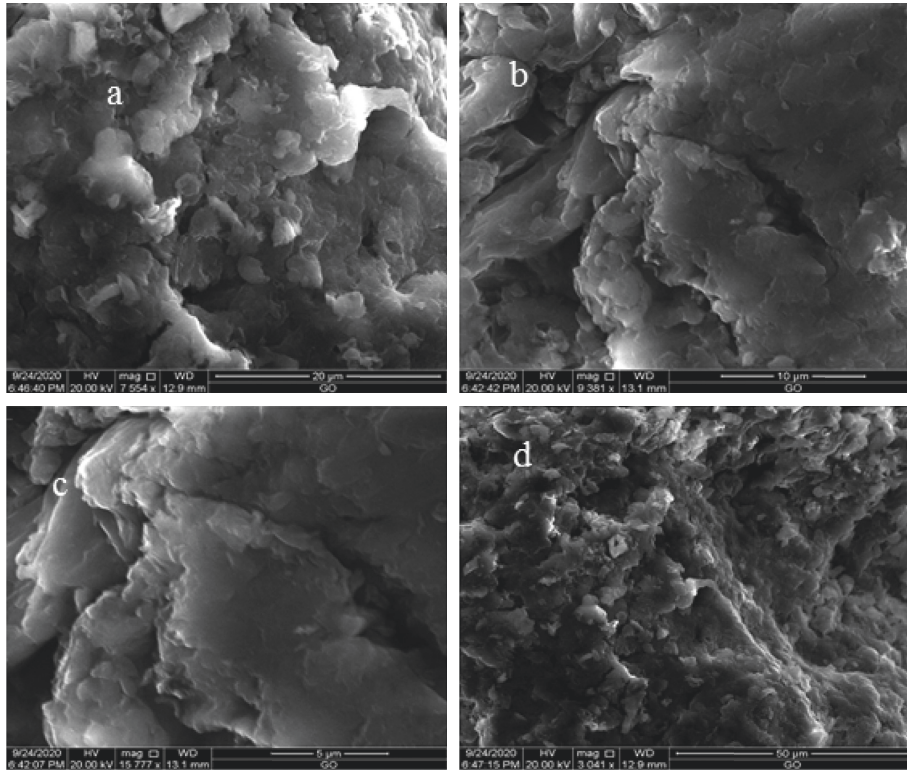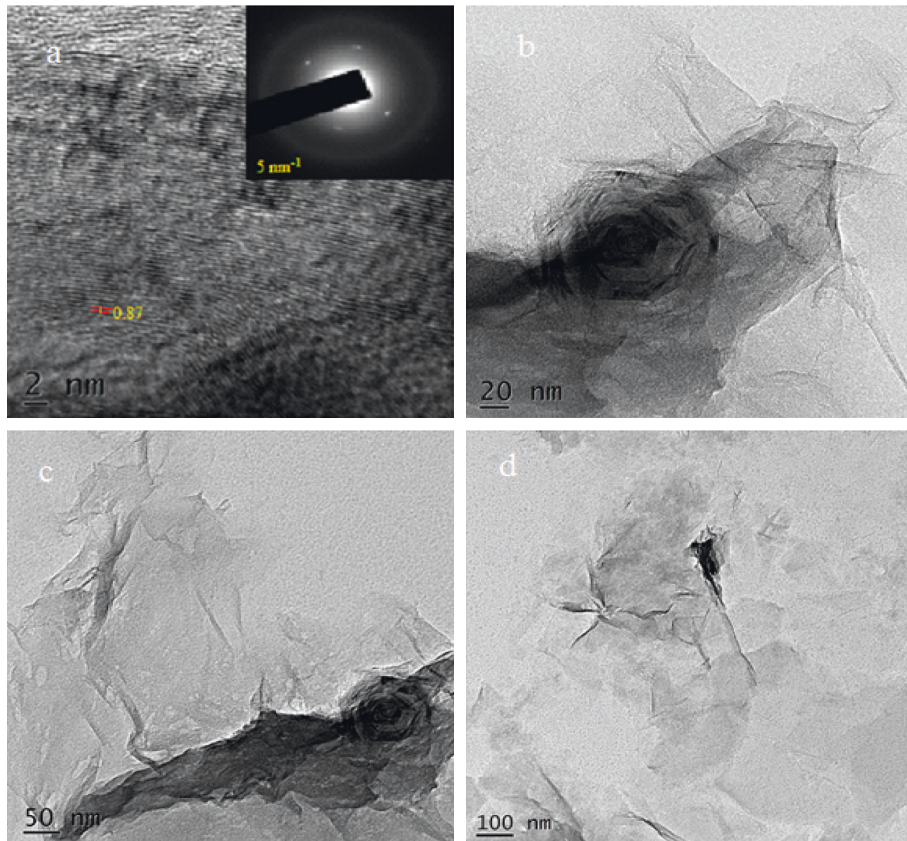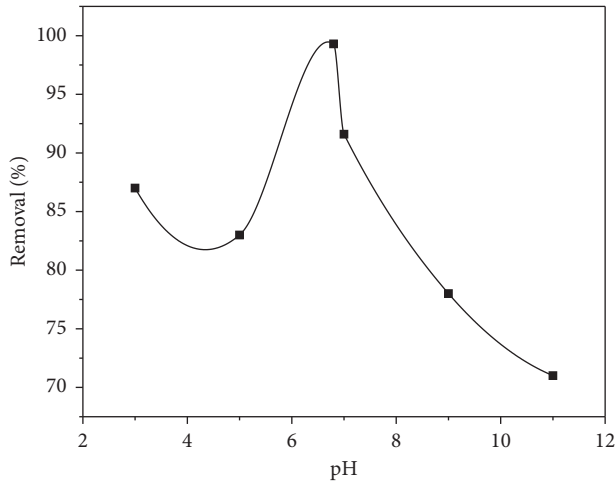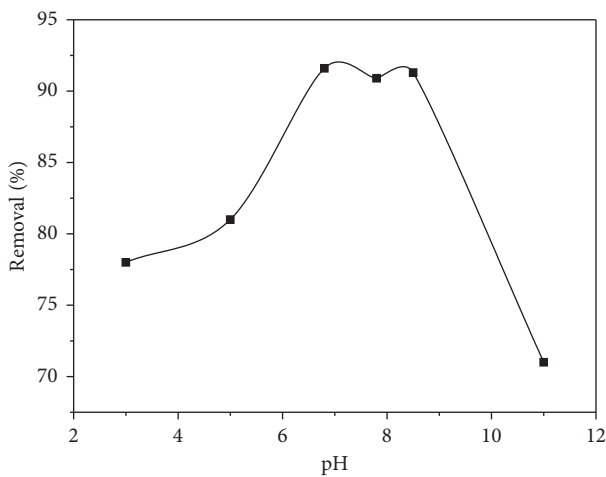
FIGURE 4: SEM morphology of GO.

FIGURE 5: (a–d) TEM image of GO along with EDAX analysis and inset is the selected area electron diffraction (SEAD) pattern of GO.

TABLE 2: The EDAX analysis results of GO nanostructure.

Element	C	O	S	Cl
Atomic (%)	62.89	35.25	1.42	0.44

FIGURE 6: Effect of pH on the removal of F^- obtained from the NaF solution.

FIGURE 8: UV–Vis of GO after fluoride ion adsorption and the inset is the UV–Vis of the sample.

FIGURE 7: Effect of pH on the removal of F^- obtained from groundwater.
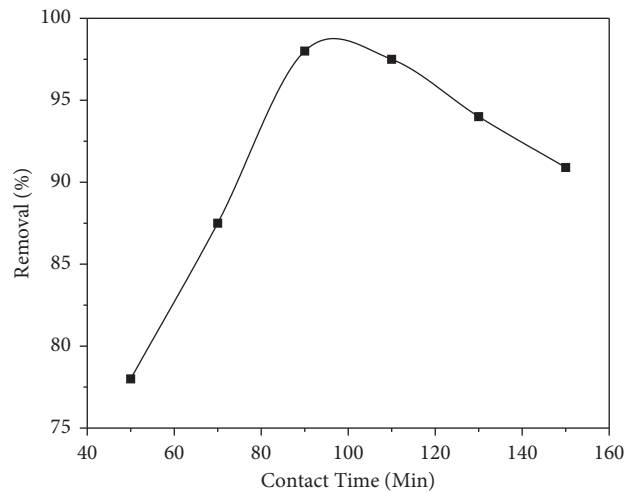
FIGURE 9: Effect of contact time on fluoride adsorption.

110, and 130, the effect of contact time on the adsorption of fluoride was studied.

The influence of contact time on the fluoride removal efficiency is shown in Figure 9. It was observed that with a constant dose of GO, the amount of fluoride adsorbed on the surface of the absorbent increases with time until the steady state was reached at 90 minutes. The maximum adsorption capacity recorded at the end of 90 minutes was found to be 98%.

3.4.3. Effect of Adsorbent Dosage. Figure 10 shows the effect of adsorbent dosage at an agitation rate of 120 rpm, agitation time of 90 minutes, and pH 6.8. The result depicted
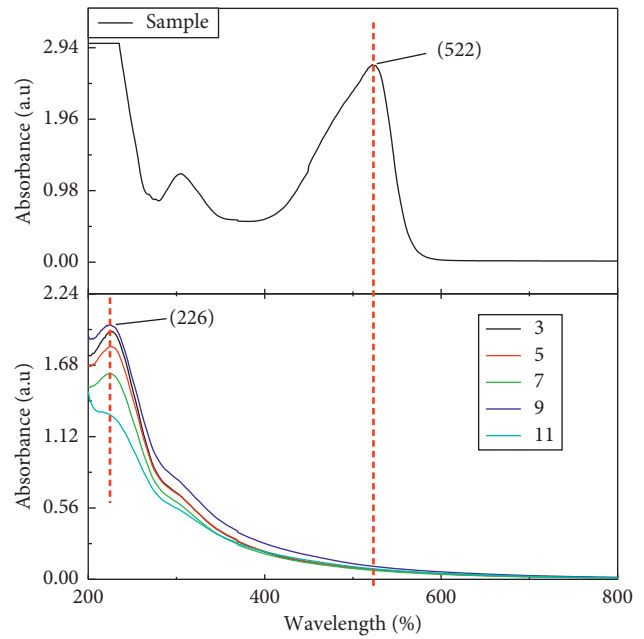
that the adsorption of fluoride by GO increases rapidly as the dosage increases up to the optimum value 0.42 mg. The adsorption capacity of GO at this dosage is 97%. Increasing the dosage beyond this value does not bring any change to the adsorption of fluoride ions.

3.4.4. Effect of Initial Concentration. The capacity of GO to adsorb fluoride was assessed using the initial concentration of fluoride ranging from 1 to 40 mg/L while the other parameters were constant. The rate of adsorption of fluoride onto GO was so fast that most of the adsorption process was completed within 30 minutes. Fluoride adsorption increased with increasing initial concentrations of fluoride and this is
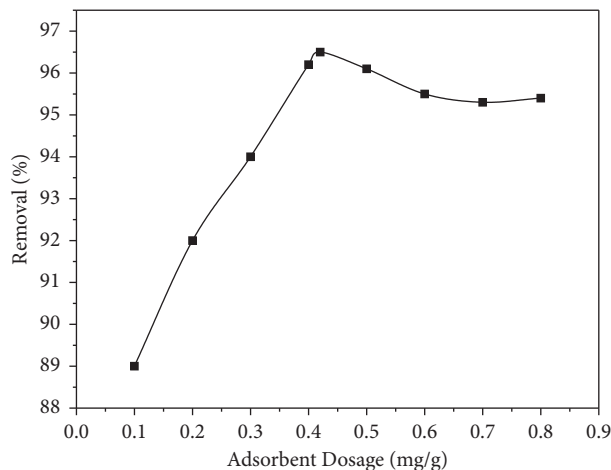
FIGURE 10: Effect of adsorbent dosage on fluoride ion adsorption.

FIGURE 11: Effects of initial fluoride concentration.

attributed to the diffusion of the adsorbate to the adsorbent surface as shown in Figure 11.

3.5. Adsorption Kinetics.

Figure 12 shows the pseudo-first-order and pseudo-second-order kinetics models of fluoride adsorption onto GO. The fluoride adsorption kinetics of GO was tested at an agitation speed of 120 rpm, adsorbent dosage of 0.42 mg/L, contact time of 90 minutes, and pH 6.8. Table 3 shows the values of K_f, K_s, K_d, and K_p experimental adsorption capacity at equilibrium $q_{e,\exp}$ and calculated adsorption capacity at equilibrium $q_{e,\text{calc}}$.

The adsorption kinetics of both pseudo-first-order (SFO) and pseudo-second-order (SSO) reactions were determined. The adsorption kinetics for the SSO reactions was found to be 0.99 for the coefficient of determination (R^2) and the sum of square errors was 0.0002. R^2 and the sum of square errors for the SFO reaction were 0.96 and 0.02, respectively, as indicated in Table 3.

The R^2 value for the SSO kinetics is larger than the corresponding R^2 value for the SFO reaction and the difference between $q_{e,\text{calc}}$ and $q_{e,\exp}$ was insignificant such that the sum of square error is very small. This shows that the SSO reaction best describes the fluoride adsorption by GO.

The absorption/diffusibility of the adsorbate into the adsorbent was determined from the intraparticle diffusion model. Using equation (12), the value of the intraparticle diffusion rate constant k_p and the value of C were obtained from the slope (m) and intercept (C) of the plot of q_e versus square root of time as in Table 3. The plot of q_t versus $t^{0.5}$, Figure 13(a) showed a nonlinear dependency over the total range, with the line not passing through the origin.

This indicates that the rate-limiting step is controlled by boundary layer diffusion. The sharp rapid increasing plot initially observed indicates the fast uptake of ions onto the GO surface which is decreased gradually due to surface saturation at equilibrium. As shown in the upper region of Figure 13(a), there is slow process which was involved in the transportation of F⁻ into the adsorbent pores. Therefore, the overall process is controlled by particles rather than pore
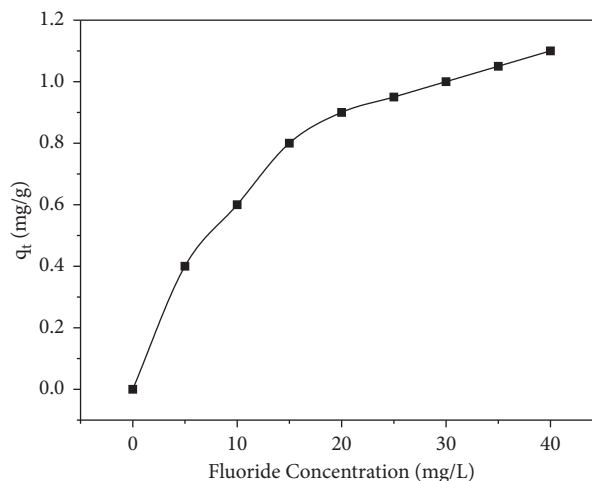
diffusion, which is also supported by the high value of R^2 shown in Table 3.

3.6. Adsorption Isotherms.

The Langmuir and Freundlich isotherms are the basic models employed to describe the adsorption isotherms using the experimentally obtained data [30, 31]. The adsorption capacity of GO was evaluated under the removal of fluoride from aqueous solutions of NaF and a real sample taken from fluoride-polluted groundwater of Dugda-Bora. The Langmuir isotherm model is suitable for monolayer adsorption, while the Freundlich isotherm model is applied for multilayer adsorption because of its heterogonous active surfaces, which have different adsorption capacities. The Langmuir and Freundlich isotherms are expressed as given in equations (14) and (15).

$$\frac{C_e}{q_e} = \frac{C_e}{q_m} + \frac{1}{bq_m}, \tag{14}$$

$$\ln q_e = \ln K_f + \frac{1}{n}\ln c_e, \tag{15}$$

where c_e is the adsorbate concentration at equilibrium (mg/L), q_e is the amount of adsorbate adsorbed per unit mass of the adsorbent at equilibrium (mg/g), q_m is the maximum adsorption capacity of the adsorbate per unit mass of adsorbent (mg/g), b is the Langmuir constant related to energy adsorption (L/mg), k_f is the Freundlich constant (mg/g) correlated to the relative adsorption capacity of the adsorbent, and n is the Freundlich exponent that describes the intensity of the adsorption. Figure 14 shows the isotherm modeling of Langmuir and Freundlich for fluoride adsorption by GO and Figure 15 shows the plot of Temkin and D–R isotherms. Table 4 shows the parameters of the Langmuir, Freundlich, and other models for the removal of fluoride by GO.

As shown in Table 4, the value of the correlation coefficient (R^2) of the Langmuir and Freundlich adsorption models was 0.96 and 0.99, respectively. Based on the data obtained from Table 4, the Freundlich isotherm depicted a
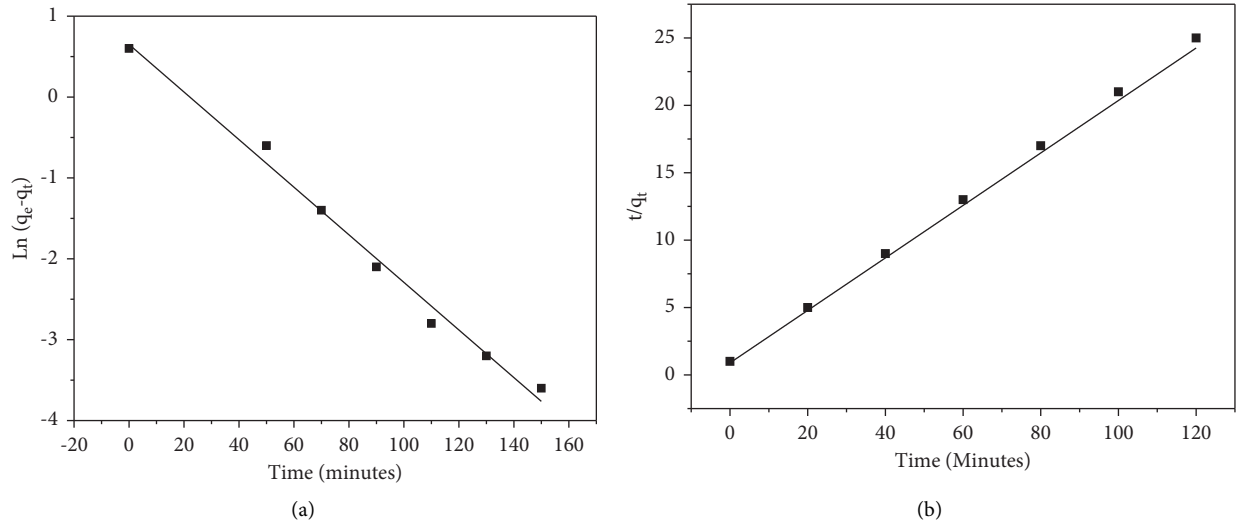
(a)

(b)

FIGURE 12: Pseudo-first-order (a) and pseudo-second-order (b) kinetics models of fluoride adsorption onto GO.

TABLE 3: The kinetics parameters for the adsorption of fluoride ions by GO.

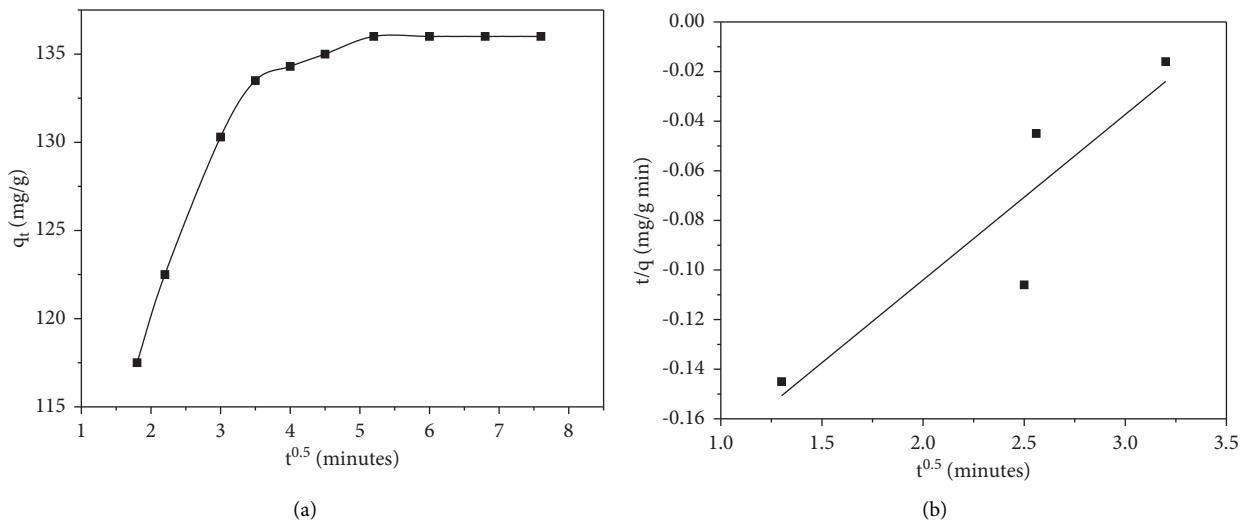|	Parameter	Value
SFO	$q_{e,\exp}$ (mg/g)	0.2263
	$q_{e,\text{calc}}$ (mg/g)	0.0920
	K_f (g/mg min)	0.0381
	R^2	0.96
SSO	$q_{e,\exp}$ (mg/g)	0.2263
	$q_{e,\text{calc}}$ (mg/g)	0.2533
	K_s (g/mg min)	0.739
	R^2	0.99
Intraparticle diffusion	K_{id1} (mg/g min$^{0.5}$)	0.0086
	C_{i1} (mg/g)	0.161
	R_1^2	0.86
	K_{id2} (mg/g min$^{0.5}$)	11.1
	C_{i2} (mg/g)	89.72
	R_2^2	0.85
	K_{id3} (mg/g min$^{0.5}$)	0.061
	C_{i3} (mg/g)	109.3
	R_3^2	0.61
Particle diffusion	k_p (mg/g min)	0.221

(a)

(b)

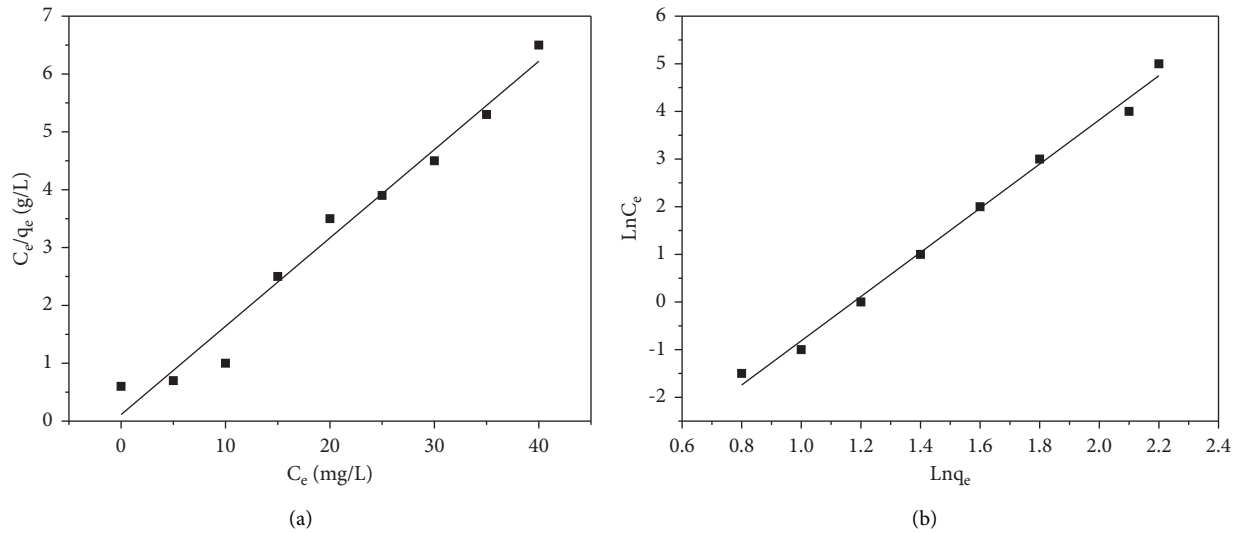FIGURE 13: A plot for (a) Weber and Morris, (b) Chanda.

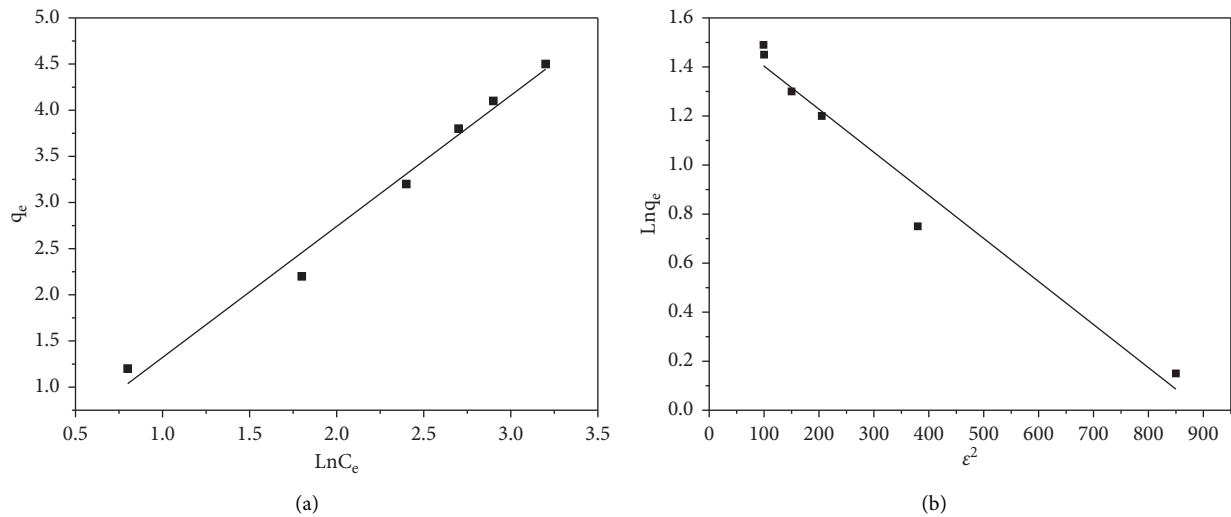FIGURE 14: Langmuir (a) and Freundlich (b) isotherm modeling of fluoride adsorption onto GO.

FIGURE 15: Temkin (a) and D–R (b) isotherm modeling of fluoride adsorption onto GO.

good fit to the experimental data. The Freundlich constant K_f and the Freundlich coefficient n were obtained from the slope and intercept as 4.61 and 4.05. The value of n shows the adsorption process is favorable. This is due to the presence of different functional groups on the surface of GO having different active sites. The maximum adsorption capacity of GO was calculated to be 301.43 mg/g.

3.7. Desorption Studies.
Desorption studies aid in determining adsorbent reusability without compromising the adsorbent's efficiency. Therefore, desorption and regeneration studies are important in adsorption studies. Desorption may occur either by thermal treatment or through suitable desorbing agents. Desorption of the F^- ions was studied in HCl solution. The adsorbent with its adsorbed adsorbate was placed in this desorption medium and stirred continuously (at a stirring rate of 700 rpm) for 15 min at room

TABLE 4: The four isotherm models' parameter values for fluoride adsorption by GO.

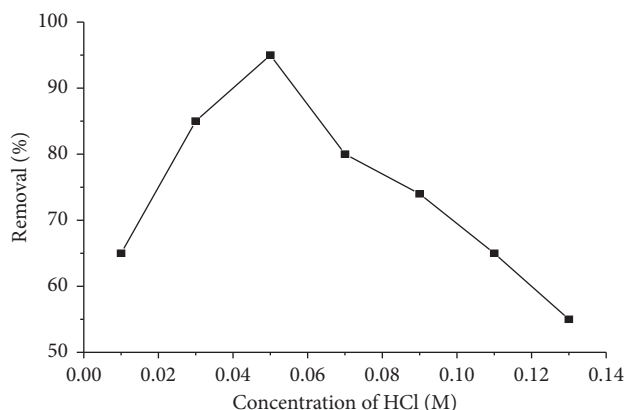| Isotherms model	Parameters	Values
	R^2	0.96
	q_m (mg g^{-1})	6
Langmuir	K_L (L mg^{-1})	0.098
	ΔG (KJ mol^{-1})	−10.6
	R_L	0.5
	R^2	0.99
Freundlich	K_F (mg g^{-1})	4.61
	n	4.05
	R^2	0.94
Tempkin	K_T (L g^{-1})	0.86
	b (J mol^{-1})	1760.4
	R^2	0.92
D–R	q_m (mg g^{-1})	5
	K_{D-R} (L mg^{-1})	−0.001
	E (KJ mol^{-1})	17

FIGURE 16: The cyclic adsorption performance of the adsorbent GO against F⁻.
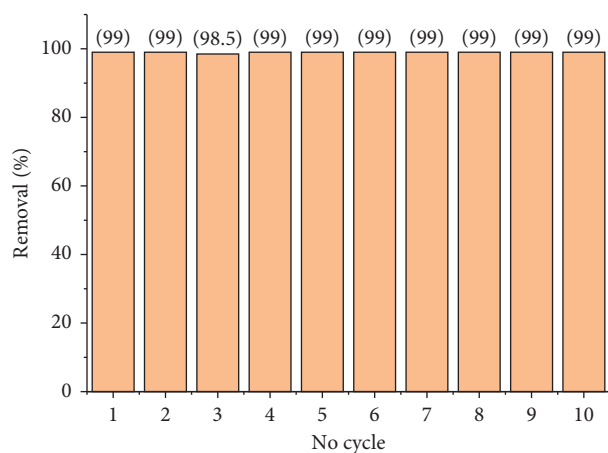
FIGURE 17: The cyclic adsorption performance of the adsorbent GO against F⁻.

4. Conclusion

Graphene oxide nanostructure was used to remove fluoride ions from groundwater by adsorption techniques. The appropriate conditions identified for the optimum adsorption activity were 120 rpm agitation rate, 90 minutes contact time, 0.42 mg/L adsorbent dosage, and pH 6.8. GO removed fluoride ions from the aqueous solutions of NaF and the real sample by 99.3% and 91.6%, respectively. The kinetics model of adsorption of fluoride onto GO was best described by the pseudo-second-order type. The research finding clearly indicated that the Freundlich isotherm is more suitable than Langmuir for the adsorption of fluoride in the groundwater by GO. The $1/n$ value of the Freundlich isotherm is 0.25 which lies between 0.1 and 1, and this indicates the adsorption processes is favorable. The adsorption capacity of GO was calculated to be maximum, indicating the adsorbent is an ideal material for the removal of fluoride from groundwater.

Data Availability

The figure data used to support the findings of this study are included within the article.

Disclosure

This work is a part of work for Adama Science and Technology University.

Conflicts of Interest

The authors declare that they have no conflicts of interest.

temperature. The desorption ratio was calculated from the amount of F⁻ ions adsorbed on the nanostructure and the final concentration of F⁻ ions in the desorption medium. To test the reusability of the adsorbent, the adsorption–desorption procedure of F⁻ ions was repeated 10 times using the same adsorbent. To regenerate after desorption, the adsorbent was washed with 0.1 M HCl and ethanol. Figure 16 shows the desorption of F⁻, and the maximum desorption efficiency was obtained in 0.05 M HCl solution as a good eluent for desorption of F⁻-loaded adsorbents.

3.8. Recyclability Study. The reusability of the adsorbent, GO nanostructure, in the adsorption of fluoride ions from groundwater was explored. After washing repeatedly with doubly distilled water, the pH of the solution was adjusted to be around 6.8 where re-adsorption of fluoride from the solution was initiated. The adsorbent was filtered and collected to dry in the oven at 60°C overnight. 0.42 mg of the powder of GO was used for the recyclability test as shown in Figure 17. The pH adjustment was done by HCl/H₂SO₄ and NaOH and the maximum adsorption capacity of GO was recovered and recorded to be 99%.

References

[1] M. A. Peres and J. A. Cury, "Drinking water quality and fluoride concentration," *Revista de Saúde Pública*, vol. 45, 2011.

[2] J.-Y. Lin, Y.-L. Chen, X.-Y. Hong, C. Huang, and C. P. Huang, "The role of fluoroaluminate complexes on the adsorption of fluoride onto hydrous alumina in aqueous solutions," *Journal of Colloid and Interface Science*, vol. 561, pp. 275–286, 2020.

[3] W. Ki, R. Si, and A. S. James, *Modified Crushed Oyster Shells for Fluoride Removal from Water*, 2020.

[4] P. S. Chandrawat, "Adsorption of fluoride in soils of Rajasthan," *International Journal of Creative Research Thoughts*, vol. 8, pp. 3039–3046, 2020.

[5] B. Thole, "Ground water contamination with fluoride and potential fluoride removal technologies for east and Southern Africa," in *Perspectives in Water Pollution Fluorosis*, 2013.

[6] D. Pratap and D. Singh, "Impact of fluoride on environment & human," *International Journal of Science, Spirituality, Business And Technology*, vol. 1, pp. 56–61, 2013.

[7] B. M. Chufa, H. C. A. Murthy, B. A. Gonfa, and T. Y. Anshebo, "Carbon nanotubes: a review on green synthesis, growth mechanism and application as a membrane filter for fluoride remediation," *Green Chemistry Letters and Reviews*, vol. 14, pp. 640–657, 2021.

[8] M. v. B. Sara Datturi, A. Kumsa, and S. Kebede, "The right to smile: fluoride and fluorosis in central rift valley (Ethiopia)," *Groundwater*, 2017.

[9] F. Mandefro, "Social accountability in the extractive industries: a review of the Ethiopian experience," *Ethiopian Journal of Business and Economics*, vol. 6, no. 1, pp. 1–72, 2017.

[10] S. Datturi, F. Van Steenbergen, M. Van Beusekom, S. Kebede, and A. Ababa, "Comparing defluoridation and safe sourcing for," *Fluoride*, vol. 48, pp. 293–314, 2015.

[11] T. C. Y. Travi, *Fluoride Contamination in the Lakes Region of the Ethiopian Rift: Origin, Mechanism and Evolution*, 1998.

[12] Z. A. Alemu, S. D. Mengesha, and T. A. Alemayehu, "Retrospective study of fluoride distribution in ethiopian drinking water sources," *Asian Journal of Applied Science and Engineering*, vol. 4, pp. 127–136, 2015.

[13] N. A. Medellin-castillo, R. Leyva-ramos, R. Ocampo-perez, R. F. Garcia de la Cruz, A. Aragon-Piña, and J. M. Martinez-Rosales, "Adsorption of fluoride from water solution on bone char," *Industrial & Engineering Chemistry Research*, vol. 46, pp. 9205–9212, 2007.

[14] M. Ghanbarian, M. Ghanbarian, A. Hossein, and T. Tabatabaie, "Enhanced fluoride removal over $MgFe_2O_4$–chitosan–CaAl nanohybrid: response surface optimization, kinetic and isotherm study," *International Journal of Biological Macromolecules*, vol. 148, pp. 574–590, 2020.

[15] N. Sahu, C. Bhan, and J. Singh, "Removal of fluoride from an aqueous solution by batch and column process using activated carbon derived from iron infused," *Environmental Engineering Research*, vol. 26, pp. 1–3, 2021.

[16] G. S. Kair and C. R. S. Faj, "Effect of fluoride in the human body," *World Scientific News*, vol. 5, pp. 12–16, 2014.

[17] M. Z. Q. Xiang, Y. Liang, L. Chen, C. Wang, B. Chen, and X. Chen, "Effect of fluoride in drinking water on children's intelligence," *Fluoride*, vol. 36, pp. 84–94, 2003.

[18] D. I. Kosik-bogacka, M. Lebiotkowski, I. Baranowska-bosiacka, I. Gutowska, and D. Chlubek, "Bone fluoride content in patients after," *Fluoride*, 2015.

[19] L. Aggeborn and M. Öhman, *The Effects of Fluoride in the Drinking Water*, 2017.

[20] A. A. Ayalew, "Development of kaolin clay as a cost-effective technology for defluoridation of groundwater," *International Journal of Chemical Engineering*, vol. 2020, Article ID 8820727, 2020.

[21] B. Karthikeyan, "Fluoride removal from aqueous solution using Psidium guajava and Mimosa pudica Leaves," *International Journal of Advanced Research Trends in Engineering and Technology*, vol. 5, 2019.

[22] M. Malakootian, M. Moosazadeh, N. Yousefi, and A. Fatehizadeh, "Fluoride removal from aqueous solution by pumice: case study on Kuhbonan water," *African Journal of Environmental Science and Technology*, vol. 5, pp. 299–306, 2011.

[23] F. Perreault, A. F. De Faria, and M. Elimelech, "Environmental applications of graphene-based nanomaterials," *The Royal Society of Chemistry*, vol. 44, pp. 5861–5896, 2015.

[24] M. Zawar, R. Nazir, A. Hamid, and E. C. Lima, "Rapid de fluoridation of drinking water by calcium carbonate nanoadsorbent: characterization, adsorption studies and application to real samples' treatment," *Water Supply*, vol. 20, pp. 667–678, 2020.

[25] M. C. Collivignarelli, A. Abbà, M. C. Miino, V. Torretta, E. C. Rada, and F. M. Caccamo, "Adsorption of fluorides in drinking water by palm residues," *Sustainable Times*, vol. 12, pp. 1–12, 2020.

[26] Y. Ku, H. Chiou, and W. Wang, "Separation Science and Technology the removal of fluoride ion from aqueous solution by a cation synthetic resin," *Separation Science and Technology*, vol. 37, pp. 89–103, 2002.

[27] J. Fito, H. Said, S. Feleke, and A. Worku, "Fluoride removal from aqueous solution onto activated carbon of Catha edulis through the adsorption treatment technology," *Environmental Systems Research*, vol. 8, pp. 1–10, 2019.

[28] T. L. Tan, P. A. P. Krusnamurthy, and S. Abdul, "Adsorptive, kinetics and regeneration studies of fluoride removal from water using zirconium-based metal organic frameworks," *RSC Advances*, vol. 10, pp. 18740–18752, 2020.

[29] U. O. Aigbe and B. Onyancha, "Removal of fluoride ions using a polypyrrole magnetic nanocomposite in fluenced by a rotating magnetic field," *RSC Advances*, vol. 10, pp. 595–609, 2020.

[30] N. Tefera, Y. Mulualem, and J. Fito, "Adsorption of fluoride from aqueous solution and groundwater onto activated carbon of avocado seeds," *Water Conservation Science and Engineering*, vol. 5, pp. 187–197, 2020.

[31] N. Xu, S. Li, W. Li, and Z. Liu, "Removal of fluoride by graphene oxide/alumina nanocomposite: adsorbent preparation, characterization, adsorption performance and mechanisms," *ChemistrySelect*, vol. 5, pp. 1818–1828, 2020.

[32] L. Ü. Meijiao, L. I. Jing, Y. Xuyu, Z. Changan, Y. Jia, and H. U. Hao, "Applications of graphene-based materials in environmental protection and detection," *Chinese Science Bulletin*, vol. 58, pp. 2698–2710, 2013.

[33] K. Yang, B. Chen, and L. Zhu, *Graphene-Coated Materials Using Silica Particles as a Framework for Highly Efficient Removal of Aromatic Pollutants in Water*, Nature Publishing Group/Nature Publishing Group, Berlin, Germany, 2015.

[34] X. Li, Y. Chen, Z. Cheng, L. Jia, S. Mo, and Z. Liu, "Ultrahigh specific surface area of graphene for eliminating subcooling of water," *Applied Energy*, vol. 130, pp. 824–829, 2014.

[35] B. M. Chufa, B. A. Gonfa, T. Y. Anshebo, and G. A. Workneh, "A novel and simplest green synthesis method of reduced graphene oxide using methanol extracted vernonia amygdalina: large-scale production," *Advances in Condensed Matter Physics*, vol. 2021, pp. 1–10, 2021.

[36] T. Fentaw and D. Worku, "Controlled synthesis, characterization and reduction of graphene oxide: a convenient method for large scale production," *Egyptian Journal of Basic and Applied Sciences*, vol. 4, pp. 74–79, 2017.

[37] D. C. Marcano, D. V. Kosynkin, J. M. Berlin, A. Sinitskii, Z. Sun, and A. Slesarev, "Improved synthesis of graphene oxide," *ACS Nano*, vol. 4, pp. 4806–4814, 2010.

[38] P. Choudhary and O. P. Choudhary, "Scanning electron microscope: advantages and disadvantages in imaging components," *International Journal of Current Microbiology and Applied Sciences*, vol. 6, pp. 1877–1882, 2017.

[39] F. Perreault, A. Fonseca De Faria, and M. Elimelech, "Environmental applications of graphene-based nanomaterials," *Chemical Society Reviews*, vol. 44, pp. 5861–5896, 2015.